Available online at www.sciencedirect.com
ScienceDirect
Trans. Nonferrous Met. Soc. China 25(2015) 2172−2180
Transactions of Nonferrous Metals Society of China
www.tnmsc.cn

Microstructures, corrosion and mechanical properties of as-cast Mg−Zn−Y−(Gd) alloys

Fei SHI[1], Chun-qing WANG[1,2], Zhong-ming ZHANG[3]

1. School of Materials Science and Engineering, Harbin Institute of Technology (Weihai), Weihai 264209, China;
2. State Key Laboratory of Advanced Welding and Joining, Harbin Institute of Technology, Harbin 150001, China;
3. School of Materials Science and Engineering, Xi'an University of Technology, Xi'an 710048, China

Received 22 December 2014; accepted 13 May 2015

Abstract: Long period stacking ordered (LPSO) structure phases were prepared by conventional solidification method in $Mg_{94}Zn_3Y_xGd_{3-x}$ (x=3, 2, 1.5, 1, mole fraction) alloys, the microstructures, corrosion and compressive mechanical properties of which were investigated, separately. The results reveal that the microstructures of the as-cast $Mg_{94}Zn_3Y_xGd_{3-x}$ alloys, with n(Zn)/n(Y+Gd)=1:1, consist of α(Mg) phase, $Mg_3Zn_3RE_2$ (W) phase, $Mg_{12}ZnRE$ (14H-LPSO) phase and a few bright cube-shaped Mg−Y−Gd phases. The formation and the distribution of LPSO-phase in the alloys can be influenced by the content of Gd. The volume fraction of 14H-LPSO phase increases first and then decreases with the increase of the Gd content. For the electrochemical impedance spectroscopy (EIS) measurement, a R(Q(R(QR))) model was used to fit the test results in 3.5% (mass fraction) NaCl solution at room temperature. The corrosion current densities of all samples are about 10^{-5} A/cm^2. When x(Gd)≤1%, Mg−Zn−Y−(Gd) alloy shows good corrosion resistance, which is better than that of the commercial AZ91D magnesium alloy. The corrosion rate increases when the Gd content is higher than 1.5%. At room temperature, the compressive properties of Mg−Zn−Y−(Gd) alloys increase remarkably with the increase of the volume fraction of LPSO phase. In addition, the pinning effect of W-phase and dispersive cube-shaped Mg−Y−Gd phase is beneficial to improving the mechanical properties of as-cast $Mg_{94}Zn_3Y_xGd_{3-x}$ alloy in deformation process.

Key words: as-cast magnesium alloy; Mg−Zn−Y−(Gd) alloy; 14H-LPSO phase; corrosion property; compressive properties

1 Introduction

Magnesium alloy is the lightest engineering material, which has high damping capacity, electromagnetic shielding characteristics, thermal conductivity, electrical conductivity, castability, dimensional stability, machinability, reproducibility and bio-compatibility [1−4]. However, the applications of as-cast Mg alloys are limited due to their poor room-temperature and elevated-temperature mechanical properties, low corrosion resistance and high machining cost [5]. Recently, a large number of studies show that different types of reinforced phases in Mg−Zn−RE alloy, such as the thermodynamically stable quasicrystalline $Mg_{30}Zn_{60}RE_{10}$ (I) phase, $Mg_3Zn_3RE_2$ (W) phase and $Mg_{12}ZnRE$ (X) phase with LPSO structure, can be obtained by adjusting compositions, preparation methods and heat treatment technology [6−8]. I-phase reinforced magnesium alloy exhibits a higher elastic modulus and a higher plasticity, but its tensile strength is relatively low [9]. LPSO reinforced magnesium alloy has already attracted a wide attention due to its superior mechanical properties [7].

Rare earth elements of Y and Gd, which have high solid solubility in Mg (12.4% and 23.5%, respectively, mass fraction) [10−12], can induce significant aging strengthening and solid solution strengthening to Mg alloys. Especially, the LPSO reinforced Mg alloys containing Gd are considered as a new type of magnesium alloys which can provide good elevated-temperature mechanical properties and corrosion properties [13]. The studies have been carried out on Mg−Gd−Zn [13−14], Mg−Gd−Zn−Zr [15] and Mg−

Foundation item: Project (51374084) supported by the National Natural Science Foundation of China, Project supported by the Power Electronics Science and Education Development Program of Delta Environmental & Educational Foundation, China; Project (2010K10-08) supported by the Science and Technology Plan (Industrial Research) of Shaanxi Province, China
Corresponding author: Chun-qing WANG; Tel: 0086-451-86418725; E-mail: wangcq@hit.edu.cn
DOI: 10.1016/S1003-6326(15)63829-8

Gd−Y−Zn−Zr [16] alloys. All of these studies were focused on the solidification microstructures and the mechanical properties [17,18]. While, a systematic research is lacked on the formation of the second phases and the corrosion behavior of LPSO reinforced Mg alloy. Hence, the research on the Mg−Zn−Gd and Mg−Zn−Y−Gd alloys needs to be improved further.

This work aims to make a systematical analysis about the effect of Gd and Y on the solidification microstructures, corrosion mechanism and compressive properties of as-cast LPSO-reinforced $Mg_{94}Zn_3Y_xGd_{3-x}$ alloys.

2 Experimental

High-purity Mg and Zn (99.9%, mass fraction), Mg−30%Y (mass fraction) and Mg−30%Gd (mass fraction) master alloys were selected as the raw materials. The ingots were prepared with the nominal compositions of $Mg_{94}Zn_3Y_3$, $Mg_{94}Zn_3Y_2Gd_1$, $Mg_{94}Zn_3Y_{1.5}Gd_{1.5}$ and $Mg_{94}Zn_3Y_1Gd_2$ (mole fraction, %) separately, by casting in 5 kW electric resistance furnace with graphite crucibles under the mixed salt protection. After the solution treatment, the melt was poured into a metallic mould at 830 °C. The actual chemical compositions of the alloys were determined by OXFORD Xpert 52R0087 type direct reading spectrometer. The nominal and actual compositions of the alloys designed in this work are presented in Table 1.

Table 1 Actual chemical compositions of as-cast $Mg_{94}Zn_3Y_xGd_{3-x}$ alloys (mass fraction, %)

Alloy	Zn	Y	Gd	Mg
$Mg_{94}Zn_3Y_3$	7.75	13.8	−	Bal.
$Mg_{94}Zn_3Y_2Gd_1$	7.62	6.43	5.71	Bal.
$Mg_{94}Zn_3Y_{1.5}Gd_{1.5}$	7.69	5.16	8.17	Bal.
$Mg_{94}Zn_3Y_1Gd_2$	7.55	3.75	11.65	Bal.

The microstructures of the specimens were observed by an optical microscope (OM, OLYMPUS LX 50) and a scanning electron microscope (SEM, AMREY−100B). The micro-area chemical compositions were analyzed by an energy dispersive spectrometer (EDS, JSM−6700F and EDAX GENESIS 2048), and the phases were identified by an X-ray diffraction (XRD, DX−2700) and a transmission electron microscope (TEM, JEM−2100). The electrochemical properties of the ingots and the compared alloy AZ91D were tested with the electrochemical workstation (CHI660a) at room temperature in 3.5% NaCl aqueous solution. A three-electrode system was established in a horizontal cell with 1 cm^2 Pt as an auxiliary electrode, saturated calomel electrode (SCE) as a reference electrode and specimen as the working electrode. The corrosion potential scan rate was 0.5 mV/s. The results of electrochemical impedance spectroscopy tests were fitted by ZSimpWin software. The compressive mechanical properties of the alloys were conducted using an Instron 2382 testing machine at room temperature with a constant strain rate of 0.5 mm/min. The cylindrical-shaped specimens with a height of 12 mm and a diameter of 8 mm were cut for compression test.

3 Results and discussion

3.1 Microstructures

The optical micrographs of the four as-cast alloys are shown in Fig. 1. According to the figures, the white block phases, the dark phases and the thin plate-like phases are found in all four kinds of alloys. However, the distribution and the volume fraction of each phase are significantly affected by the mole ratio of Y to Gd. The number of thin plate-like phase firstly increases and then decreases with the increase of Gd content. Conversely, the grain size of the white block phase decreases at the beginning and then increases. The dendrites are finer in size in $Mg_{94}Zn_3Y_{1.5}Gd_{1.5}$ alloy, and the coarser dendrites can be found in $Mg_{94}Zn_3Y_3$ alloy.

The SEM backscatter electron images (BEIs) and EDS results of various phases in $Mg_{94}Zn_3Y_3$, $Mg_{94}Zn_3Y_2Gd_1$, $Mg_{94}Zn_3Y_{1.5}Gd_{1.5}$ and $Mg_{94}Zn_3Y_1Gd_2$ cast alloys are presented in Fig. 2 and Table 2, respectively. It shows that the black phase is α(Mg) solid solution. The mole ratio of n(Mg):n(Zn):n(RE) in the gray plate-like phases (marked as *C*, *G*, *J* and *M* in Fig. 2) is about 12:1:1, and it is identified that this component is similar to $Mg_{12}ZnRE$ which is the chemical formula of LPSO-phase. The mole ratio of Zn to RE is found to be around 1.5 in the lamellar eutectic phase, thus it can be identified as $Mg_3Zn_3RE_2$ phase (RE represents Y and Gd). A few bright cube-shaped phases randomly distributed in Mg−Zn−Y−(Gd) alloys could be found in Figs. 2(a), (c) and (d). EDS results present that Mg, Y and Gd components are contained in these phases with almost no Zn at all. Therefore, the phases are determined as Mg−RE phases, the n(Mg)/n(RE) ratio of which is close to 3. Analysis indicates that moderately increasing the amount of Gd can enhance the nucleation sites, so as to promote the nucleation and the growth of LPSO-phase. The microstructures of all the alloys also show that increasing the volume fraction of LPSO-phase can decrease the volume fraction of *W*-phase and refine α(Mg) dendrites.

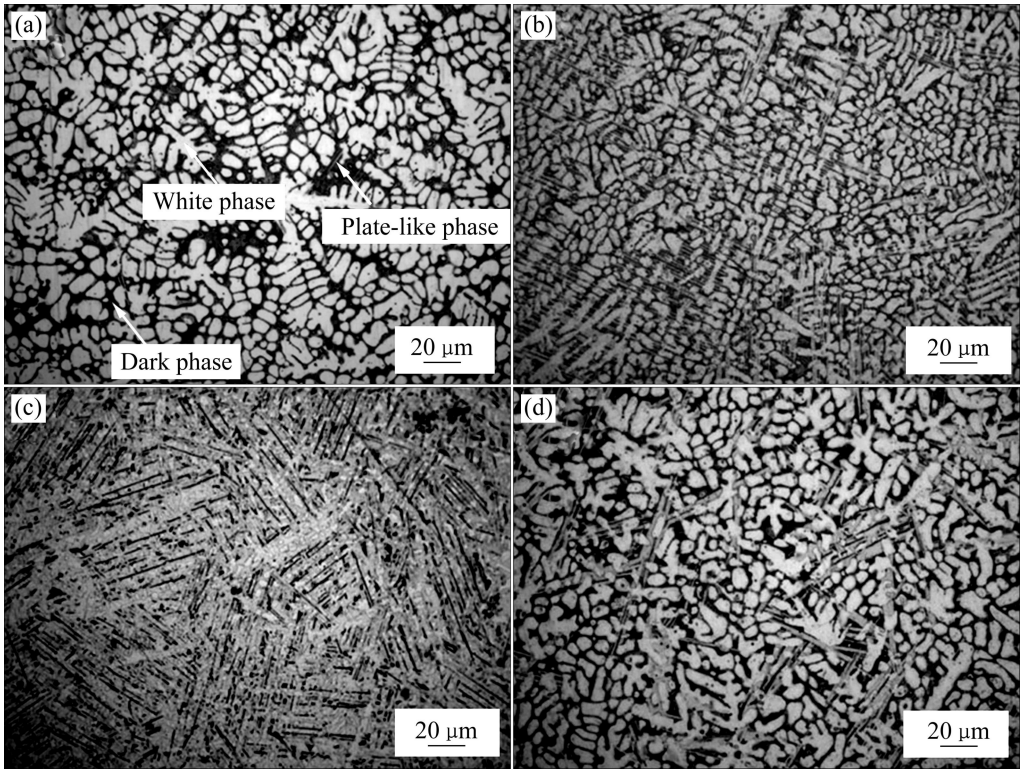


Fig. 1 Optical micrographs of as-cast alloys: (a) $Mg_{94}Zn_3Y_3$; (b) $Mg_{94}Zn_3Y_2Gd_1$; (c) $Mg_{94}Zn_3Y_{1.5}Gd_{1.5}$; (d) $Mg_{94}Zn_3Y_1Gd_2$

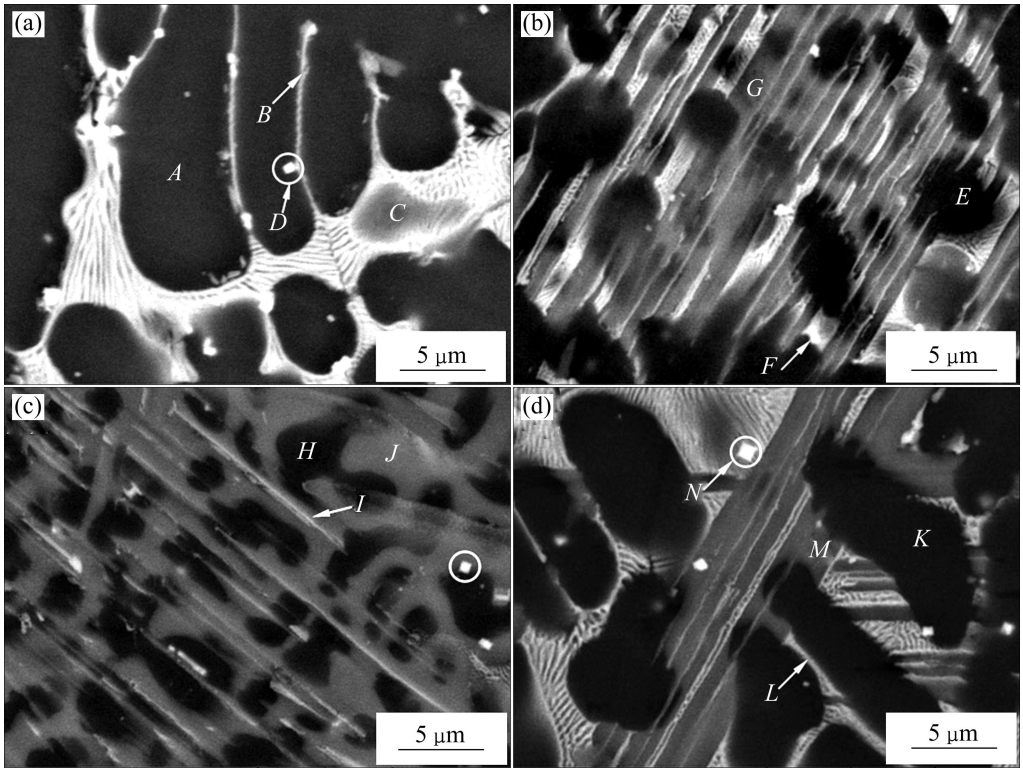


Fig. 2 SEM backscatter electron images of as-cast $Mg_{94}Zn_3Y_xGd_{3-x}$ alloys: (a) $Mg_{94}Zn_3Y_3$; (b) $Mg_{94}Zn_3Y_2Gd_1$; (c) $Mg_{94}Zn_3Y_{1.5}Gd_{1.5}$; (d) $Mg_{94}Zn_3Y_1Gd_2$

The XRD diffraction patterns of the four alloys are presented in Fig. 3. There are three kinds of diffraction peaks, corresponding to α(Mg), $Mg_3Zn_3RE_2$(W) and $Mg_{12}ZnRE$(X) phases. The diffraction pattern of as-cast

Table 2 EDS results of different phases in as-cast $Mg_{94}Zn_3Y_xGd_{3-x}$ alloys

Alloy	Position	Mole fraction/%			
		Mg	Zn	Y	Gd
$Mg_{94}Zn_3Y_3$	*A*	98.75	0.68	0.57	−
	B	64.26	21.81	13.94	−
	C	87.03	6.52	6.45	−
	D	69.46	0.81	29.72	−
$Mg_{94}Zn_3Y_2Gd_1$	*E*	97.94	0.95	0.62	0.48
	F	65.56	21.21	9.15	4.08
	G	87.09	6.52	4.32	2.07
$Mg_{94}Zn_3Y_{1.5}Gd_{1.5}$	*H*	97.94	0.63	1.56	0.17
	I	65.86	20.74	9.58	3.82
	J	87.77	5.83	4.08	2.31
$Mg_{94}Zn_3Y_1Gd_2$	*K*	98.47	0.51	0.35	0.67
	L	62.21	23.37	9.77	4.64
	M	87.73	6.25	4.68	1.34
	N	75.06	0.61	10.68	13.65

$Mg_{94}Zn_3Y_3$ alloy contains Mg, $Mg_3Zn_3Y_2$ and $Mg_{12}ZnY$ phases, as shown in Fig. 3(a). After adding Gd, the lattice parameters of as-cast $Mg_{94}Zn_3Y_2Gd_1$, $Mg_{94}Zn_3Y_{1.5}Gd_{1.5}$ and $Mg_{94}Zn_3Y_1Gd_2$ alloys are slightly changed due to Gd dissolved in the Mg matrix and compounds. Therefore, the diffraction peaks in XRD spectra have a slight deviation. In contrast, the pattern of $Mg_{94}Zn_3Y_{1.5}Gd_{1.5}$ alloy shows the weakest peak for *W*-phase because of the smallest volume fraction of this phase, as seen in Fig. 3(c). Due to the very low volume fraction of Mg−RE phase, the diffraction peaks of Mg−RE phase cannot be found in this test.

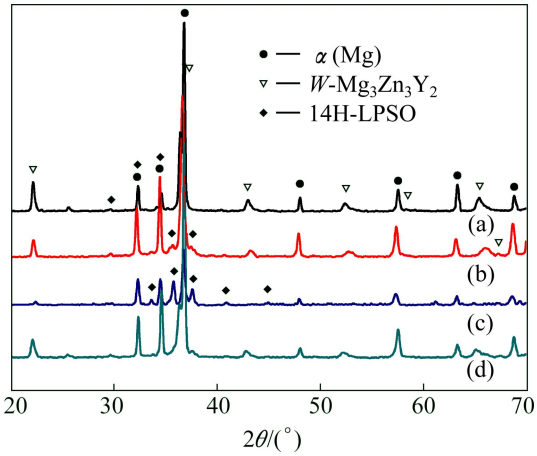


Fig. 3 XRD patterns of Mg−Zn−Y(−Gd) alloys: (a) $Mg_{94}Zn_3Y_3$; (b) $Mg_{94}Zn_3Y_2Gd_1$; (c) $Mg_{94}Zn_3Y_{1.5}Gd_{1.5}$; (d) $Mg_{94}Zn_3Y_1Gd_2$

The TEM image of the bright cube-shaped phase in as-cast $Mg_{94}Zn_3Y_3$ alloy is shown in Fig. 4(a). The size of this phase is less than 1 μm, and the corresponding SAED pattern, as shown in Fig. 4(b), reveals that the cube-shaped phase has a face-centered cubic (FCC) structure. But the lattice parameter is different from that of Mg_3Gd or *W* type phases. Figure 4(c) presents the SAED pattern of the matrix phase in $Mg_{94}Zn_3Y_3$ alloy with a hexagonal Mg crystal structure. The BF-TEM image of the fishbone-shaped phase and the corresponding SAED pattern with the electron beam (EB) taken along [001] are presented in Figs. 4(d) and (e), respectively. It confirms that this phase is *W*-phase with a face-centered cubic (FCC) structure. Figure 4(f) shows a TEM micrograph and SAED pattern of the lamellar phase in as-cast $Mg_{94}Zn_3Y_{1.5}Gd_{1.5}$ alloy. The SAED pattern analysis indicates that the lamellar phase has

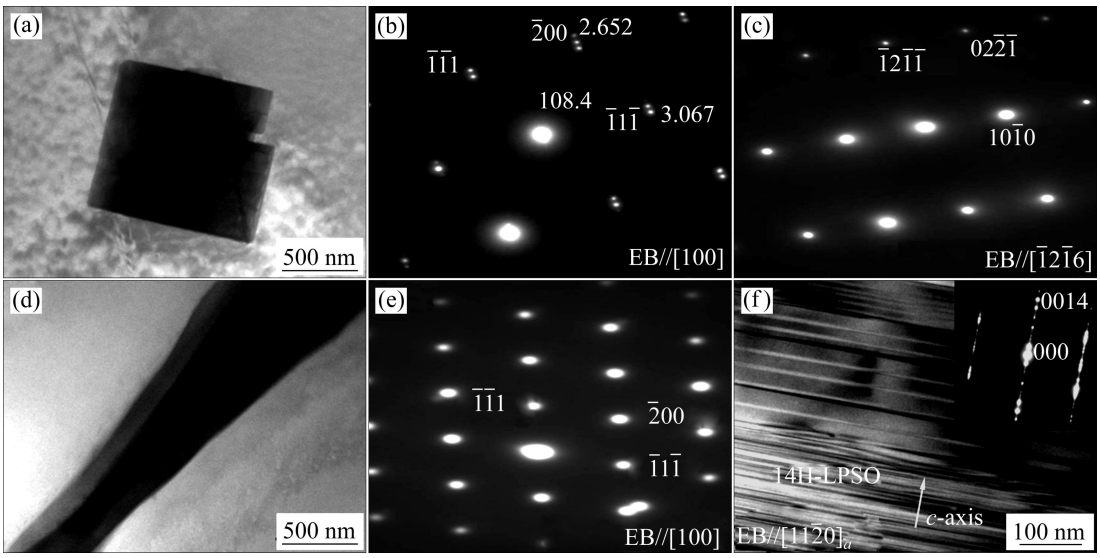


Fig. 4 TEM micrographs and corresponding SAED patterns of cube-shaped phase (a, b), *α*(Mg) matrix phase(c), *W*-phase in as-cast $Mg_{94}Zn_3Y_3$ alloy (d, e) and lamellar 14H-LPSO structure phase (f) in as-cast $Mg_{94}Zn_3Y_{1.5}Gd_{1.5}$ alloy

14H-LPSO structure with incident EB parallel to the direction of $[11\bar{2}0]_{\alpha}$.

3.2 Corrosion resistance

In order to determine the corrosion behavior of LPSO-enhanced magnesium alloys, the samples were immersed in 3.5% NaCl solution at an open circuit potential. The potentio-dynamic polarization curves of different samples were collected, as shown in Fig. 5. Tafel curves of the samples accord with the law of activation control in anode region and cathode region at the initial corrosion stage, with no passivation phenomenon occurred. Moreover, the calculated corrosion potential and corrosion current density from the polarization curves are summarized in Table 3. The corrosion potential of $Mg_{94}Zn_3Y_3$ alloy is the most positive in comparison with that of as-cast $Mg_{94}Zn_3Y_2Gd_1$, $Mg_{94}Zn_3Y_{1.5}Gd_{1.5}$ and $Mg_{94}Zn_3Y_1Gd_2$ alloys. And with the increasing content of Gd, the corrosion potential decreases from −1.524 V to −1.537 V. However, φ_{corr} of all samples are higher than that of commercial AZ91D magnesium alloy, meanwhile, the corrosion current density of samples reaches the same order of magnitude. The J_{corr} values of $Mg_{94}Zn_3Y_3$ and $Mg_{94}Zn_3Y_2Gd_1$ alloys are 3.988×10^{-5} A/cm^2 and 4.627×10^{-5} A/cm^2, respectively, which are lower than that of AZ91D alloy. When the content of Gd is up to1.5% and 2.0%, the J_{corr} is slightly higher than that of AZ91D alloy.

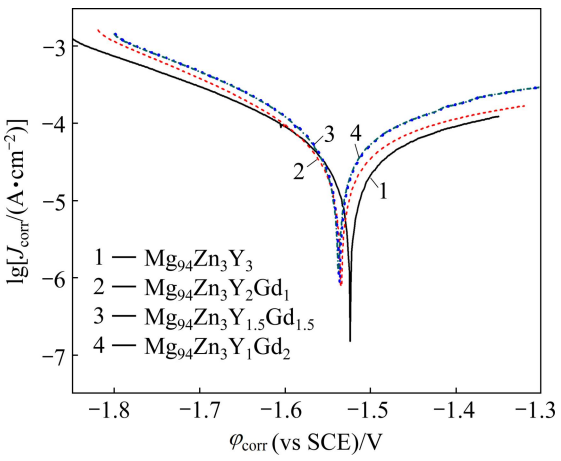


Fig. 5 Polarization behavior of as-cast $Mg_{94}Zn_3Y_xGd_{3-x}$ alloys tested in 3.5% NaCl solution

Table 3 Corrosion potential and corrosion current density of samples eroded in 3.5% NaCl solution

Alloy	J_{corr}/(A·cm^{-2})	φ_{corr}(vs SCE)/V
$Mg_{94}Zn_3Y_3$	3.988×10^{-5}	−1.524
$Mg_{94}Zn_3Y_2Gd_1$	4.627×10^{-5}	−1.534
$Mg_{94}Zn_3Y_{1.5}Gd_{1.5}$	6.352×10^{-5}	−1.536
$Mg_{94}Zn_3Y_1Gd_2$	6.392×10^{-5}	−1.537
Commercial AZ91D	4.701×10^{-5}	−1.960

The EIS spectra of the as-cast Mg−Zn−Y−(Gd) alloys and AZ91D alloy were tested within the frequency range of $0.1-10^5$ Hz, and the fitting results are shown in Fig. 6. The fitting equivalent circuit of EIS spectra for as-cast $Mg_{94}Zn_3Y_xGd_{3-x}$ alloys is given in Fig. 7. According to Fig. 6(a), the Nyquist plots of all the as-cast $Mg_{94}Zn_3Y_xGd_{3-x}$ alloys show a capacitive loop at high frequency and a capacitive loop at medium frequency. This indicates that the alloys have the same electrochemical corrosion mechanism, but different corrosion resistances. At high-frequency region, the capacitive loop radius of $Mg_{94}Zn_3Y_3$ alloy is the biggest, indicating the highest impedance value and the lowest corrosion rate. Meanwhile, with the increasing content of Gd, the capacitive loop radius of Mg−Zn−Y−Gd alloys decreases gradually, as shown in the inset in Fig. 6(a). At medium-frequency region, $Mg_{94}Zn_3Y_3$ alloy also exhibits good corrosion ability. The impedance value of as-cast $Mg_{94}Zn_3Y_2Gd_1$ alloy is slightly smaller than that of the former. With the increasing amount of Gd, the corrosion properties of Mg−Zn−Y−Gd alloys decrease significantly. The results are consistent with those of polarization behavior. As shown in Fig. 6(b), the Bode plots of the samples show a time constant at high frequency and medium frequency in the electrode system, respectively. The impedance expression of as-cast Mg−Zn−Y−(Gd) alloys eroded in 3.5% NaCl solution is

$$Z=R_s+\left\{(j\omega C_{d1})^n+\left\{R_f+\left[(j\omega C_{d2})^n+\frac{1}{R_r}\right]^{-1}\right\}^{-1}\right\}^{-1} \quad (1)$$

where R_s is the solution resistance; R_f is the film resistance; R_r is the reaction resistance of Mg alloy; the value of R_f+R_r stands for the corrosion properties of Mg−Zn−Y−(Gd) alloys; C_{d1} is the capacitance of the oxide film and the corrosion solution; C_{d2} is the reaction capacitance of Mg alloy matrix under the oxide film.

The schematic diagram of the as-cast $Mg_{94}Zn_3Y_xGd_{3-x}$ (x=3, 2, 1.5, 1) alloys is shown in Fig. 8 to explain the corrosion process. Considering both the analysis of OM and SEM, the Mg-based oxide film is formed firstly on the α(Mg) solid solution and Mg-rich phase, as shown in Fig. 8(a). The capacitive loop in high frequency region of EIS is caused by the reaction of oxide film and corrosion medium. When Mg^{2+} reacts with OH^- to form $Mg(OH)_2$ precipitate, the barrier effect of the surface layer to corrosion medium will be fortified, as shown in Fig. 8(b). However, the Cl^- can continue to penetrate this oxide layer and reach the metal substrate

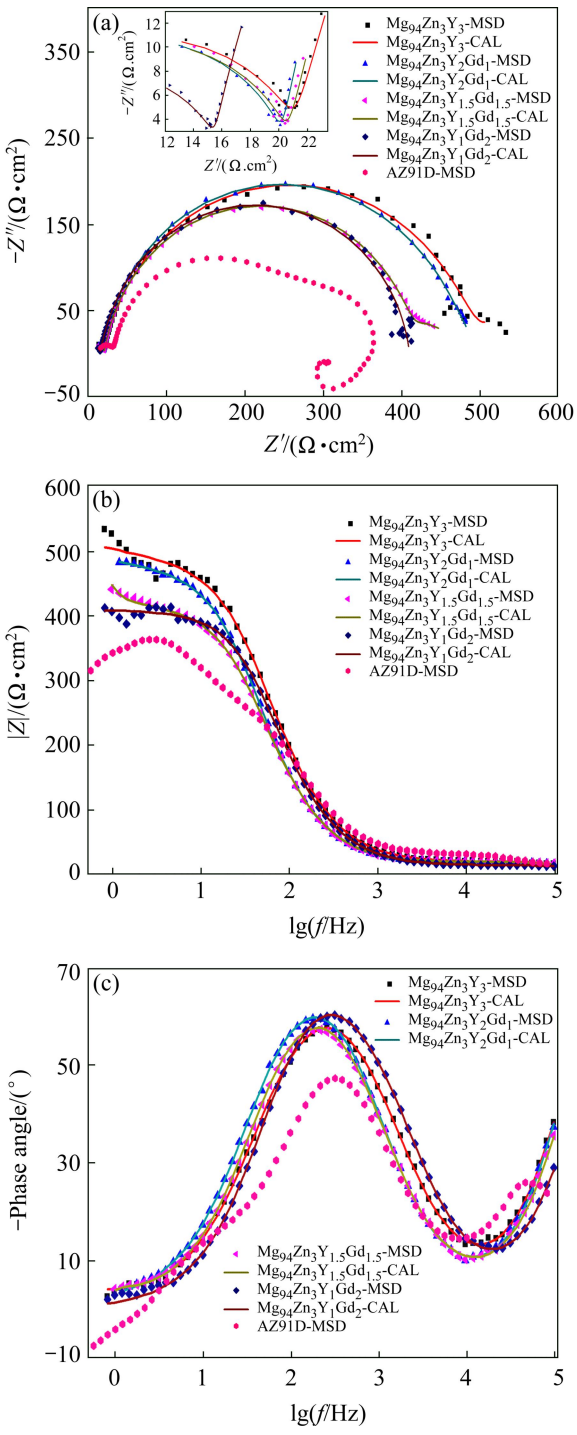


Fig. 6 EIS spectra for as-cast $Mg_{94}Zn_3Y_xGd_{3-x}$ alloys and AZ91D alloy eroded in 3.5% NaCl solution: (a) Nyquist plots; (b) Bode plots; (c) Phase angle-lg*f* plots

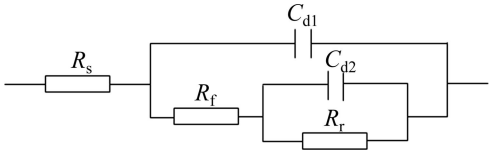


Fig. 7 Equivalent circuit of EIS spectra for as-cast $Mg_{94}Zn_3Y_xGd_{3-x}$ alloys

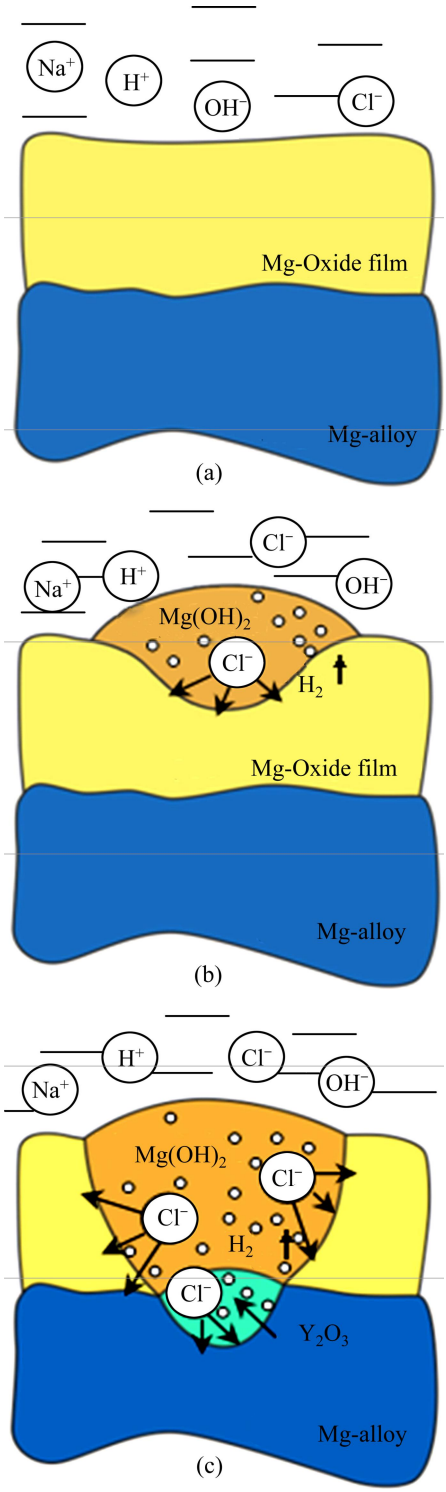


Fig. 8 Schematic drawings of as-cast Mg−Zn−Y−(Gd) alloys eroded in 3.5% NaCl solution: (a) Oxide film on Mg alloy; (b) Formation process of $Mg(OH)_2$ precipitate and H_2 gas; (c) Penetration of Cl^- and formation of Y_2O_3

due to its small volume and strong penetration ability in the corrosive medium [19]. The capacitive loop in medium frequency region of EIS is caused by the corrosion reaction of metal substrate. Generally, the higher impedance value means the lower corrosion rate.

The Y atoms in *W*-phase, LPSO phase and Mg−RE phase are able to generate stable Y^{3+} in the corrosion process [20], thereafter the corrosion products Y_2O_3 will cover on the surface of Mg alloy and corrosion pits, as shown in Fig. 8(c). Y_2O_3 is insensitive to corrosion medium due to its lower chemical activity, which can enhance the protection for the Mg alloy [21]. However, with the soluble $MgCl_2$ which inhibits the formation of oxide layer formed by the reaction of Mg^{2+} and Cl^-, there is a competition between the formation and destruction of the corrosion product in corrosion process. In Mg−Zn−Y−Gd alloys, the galvanic corrosion can be accelerated, because the amount of alloying elements is increased in α(Mg) matrix and the second phases, and also because Gd has a high electrode potential (−2.397 V) [22,23]. The results indicate that Gd can reduce the corrosion of LPSO-enhanced Mg−Zn−Y−(Gd) alloys.

3.3 Compressive mechanical properties

The compressive stress−strain curves of the four alloys at room temperature are shown in Fig. 9. The ultimate compressive stress, compressive yield stress and compression ratio of $Mg_{94}Zn_3Y_3$ cast alloy are 350 MPa, 200 MPa and 12%, respectively. In as-cast $Mg_{94}Zn_3Y_{1.5}Gd_{1.5}$ alloy, the stress increases obviously with the increasing strain, which could be up to 414 MPa. The compressive yield stress and compression ratio of this alloy are 230 MPa and 18.2%, respectively, which exhibits an excellent compressive mechanical properties. In contrast to $Mg_{94}Zn_3Y_3$ alloy, the compression rate of $Mg_{94}Zn_3Y_{1.5}Gd_{1.5}$ alloy is raised by 52%. The morphologies of shear fracture for both $Mg_{94}Zn_3Y_2Gd_1$ and $Mg_{94}Zn_3Y_{1.5}Gd_{1.5}$ alloys are shown in Fig. 10. The amount of the plastic deformation of as-cast $Mg_{94}Zn_3Y_2Gd_1$ alloy is lower than that of as-cast $Mg_{94}Zn_3Y_{1.5}Gd_{1.5}$ alloy, due to the pinning effect of *W*-phase and the less volume fraction of LPSO-phase. With the compressive stress loading, the deformation of

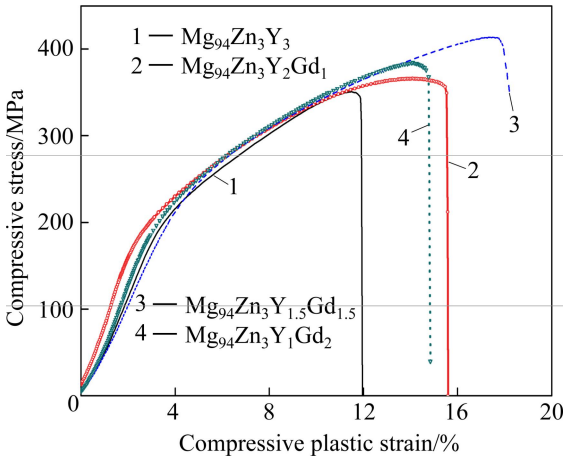


Fig. 9 Compressive stress−strain curves of alloys tested at room temperature

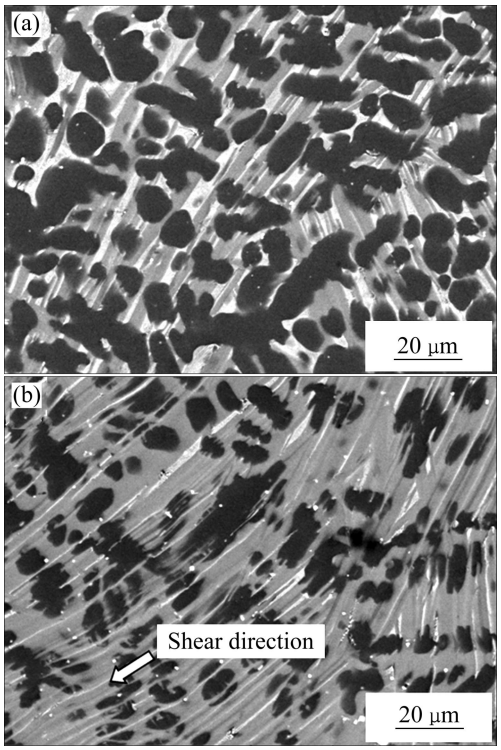


Fig. 10 Compression fracture morphologies of as-cast $Mg_{94}Zn_3Y_2Gd_1$ alloy (a) and $Mg_{94}Zn_3Y_{1.5}Gd_{1.5}$ alloy (b)

LPSO-phase is parallel to the shear direction, as shown in Fig. 10(b).

Figure 11 shows the compressive mechanical properties related to the Gd content in as-cast $Mg_{94}Zn_3Y_xGd_{3-x}$ alloys. With the increase of Gd content, the ultimate compressive stress and compressive plastic strain of $Mg_{94}Zn_3Y_2Gd_1$ and $Mg_{94}Zn_3Y_{1.5}Gd_{1.5}$ alloys increase significantly, while the properties of $Mg_{94}Zn_3Y_1Gd_2$ alloy decrease. In this work, the volume fractions of LPSO-phase in the as-cast samples follow the order: $Mg_{94}Zn_3Y_{1.5}Gd_{1.5}$>$Mg_{94}Zn_3Y_2Gd_1$>$Mg_{94}Zn_3Y_1Gd_2$>$Mg_{94}Zn_3Y_3$, as shown in Fig. 2. This result indicates that there is a close relation between the compressive mechanical properties of the alloys and the volume fraction of LPSO-phase. Normally, most magnesium alloys have less independent slip systems due to the hexagonal crystal structure, which could induce the poor plastic deformation ability at room temperature [24]. However, in this work, the compressive plastic strain and stress of LPSO-enhanced Mg−Zn−Y−(Gd) alloys are improved, which can be explained by the following three aspects. Firstly, LPSO structure itself is a kind of stacking fault (SF) which undermines the integrity and the normal crystalline periodicity, so the stacking fault energy of the crystal increases [7]. Therefore, it requires a higher load to drive the dislocation slip in plastic deformation process. Secondly, with the increase of the volume fraction of

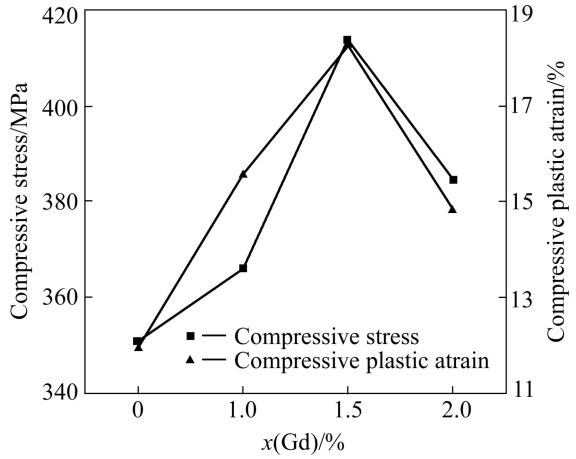


Fig. 11 Relationship between compressive mechanical properties and Gd content in as-cast $Mg_{94}Zn_3Y_xGd_{3-x}$ alloys

LPSO-phase, the grain size of α(Mg) matrix can be refined, which produces a large accumulation of grain boundaries. The Hall−Petch formula analysis shows that grain refinement can significantly increase the yield strength of magnesium alloys [25]. During the plastic deformation, the dislocations can pile up at grain boundaries and increase the energy of dislocations bypassing grain boundaries, thus forming the grain boundary strengthening. In addition, the pinning effect of the second phases, such as eutectic *W*-phase and Mg−RE phase, also hinders the slipping and climbing of dislocations [7,26,27]. Therefore, good compressive mechanical properties of LPSO-enhanced magnesium alloy are attributed to the coupling effect of the second phase strengthening, the dispersion strengthening, the fine grain strengthening and the grain boundary strengthening.

4 Conclusions

1) Microstructures of as-cast $Mg_{94}Zn_3Y_3$, $Mg_{94}Zn_3Y_2Gd_1$, $Mg_{94}Zn_3Y_{1.5}Gd_{1.5}$ and $Mg_{94}Zn_3Y_1Gd_2$ alloys mainly consist of α(Mg) solid solution, 14H-LPSO phase, $Mg_3Zn_3RE_2$ phase and few cubic-shaped Mg−RE phases. The volume fraction of LPSO-phase is affected significantly by the Gd content. When the Gd content in the alloy is 1.5%, the volume fraction of LPSO-phase can reach up to 80%.

2) The same electrochemical corrosion mechanism in the as-cast $Mg_{94}Zn_3Y_xGd_{3-x}$ (x=3, 2, 1.5, 1) alloys is investigated. The corrosion process is controlled by the electrochemical reaction of the oxide film and the Mg metal substrate. Galvanic corrosion can be accelerated in Mg−Zn−Y−Gd alloys by the higher chemical activity of Gd and the more alloying elements in α(Mg) and the second phases. Thus, the corrosion resistance of the alloys decreases.

3) In compression tests at room temperature, the as-cast $Mg_{94}Zn_3Y_xGd_{3-x}$ alloys exhibit good compressive mechanical properties, mainly due to the lamellar 14H-LPSO structure phase strengthening. In addition, the dispersion strengthening, fine grain strengthening and grain boundary strengthening also contribute to the good mechanical properties of the alloys. The ultimate compressive stress, compressive yield stress and compressive plastic strain of as-cast $Mg_{94}Zn_3Y_{1.5}Gd_{1.5}$ alloy are 414 MPa, 230 MPa and 18.2%, respectively.

References

[1] SEIFZADEH D, BEZAATPOUR A, ASADPOUR JOGHANI R. Corrosion inhibition effect of N, N′-bis (2-pyridymethylidene)-1, 2-diiminoethane on AZ91D magnesium alloy in acidic media [J]. Transactions of Nonferrous Metals Society of China, 2014, 24(11): 3441−3451.

[2] BERGE F, KRÜGER L, OUAZIZ H, ULLRICH C. Influence of temperature and strain rate on flow stress behavior of twin-roll cast, rolled and heat-treated AZ31 magnesium alloys [J]. Transactions of Nonferrous Metals Society of China, 2015, 25(1): 1−13.

[3] LUO A A, SACHDEV A K. Applications of magnesium alloys in automotive engineering [M]// Advances in Wrought Magnesium Alloys. Philadelphia: Woodhead Publishing, , 2012: 393−426.

[4] LI Nan, ZHENG Yu-feng. Novel magnesium alloys developed for biomedical application: A review [J]. Journal of Materials Science and Technology, 2013, 29(6): 489−502.

[5] XU Yan, HU Lian-xi, SUN Yu, JIA Jian-bo, JIANG Ju-fu, MA Qing-guo. Microstructure and mechanical properties of AZ61 magnesium alloy prepared by repetitive upsetting-extrusion [J]. Transactions of Nonferrous Metals Society of China, 2015, 25(2): 381−388.

[6] LUO Z P, ZHANG S Q, TANG Y L, ZHAO D S. Quasicrystals in as-cast Mg−Zn−RE alloys [J]. Scripta Metallurgica et Materialia, 1993, 28(12): 1513−1518.

[7] KAWAMURA Y, HAYASHI K, INOUE A, MASUMOTO T. Rapidly solidified powder metallurgy $Mg_{97}Zn_1Y$ alloys with excellent tensile yield strength above 600 MPa [J]. Materials Transactions, 2001, 42(7): 1172−1176.

[8] SHI Fei, YU Yuan-chun, GUO Xue-feng, ZHANG Zhong-min, LI Ying-ying. Corrosion behavior of as-cast $Mg_{68}Zn_{28}Y_4$ alloy with I-phase [J]. Transactions of Nonferrous Metals Society of China, 2009, 19(5): 1093−1097.

[9] YANG Wen-peng, GUO Xue-feng, LU Zheng-xin. TEM microstructure of rapidly solidified Mg−6Zn−1Y−1Ce [J]. Transactions of Nonferrous Metals Society of China, 2012, 22(4): 786−792.

[10] ROKHLIN L L. Magnesium alloys containing rare earth metals: Structure and properties [M]. London: Taylor & Francis, 2003.

[11] NIE J F, MUDDLE B C. Characterisation of strengthening precipitate phases in a Mg−Y−Nd alloy [J]. Acta Mater, 2000, 48: 1691−1703.

[12] FEYERABEND F, FISCHER J, HOLTZ J, WITTE F, WILLUMEIT R, DRUCKER H, VOGT C, HORT N. Evaluation of short-term effects of rare earth and other elements used in magnesium alloys on primary cells and cell lines [J]. Acta Biomaterialia, 2010, 6(5): 1834−1842.

[13] SRINIVASAN A, HUANG Y, MENDIS C L, BLAWERT C, KAINER F U, HORT N. Investigations on microstructures, mechanical and corrosion properties of Mg−Gd−Zn alloys [J]. Materials Science and Engineering A, 2014, 595: 224−234.

[14] ZHEN R, SUN Y S, XUE F, SUN J, BAI J. Effect of heat treatment on the microstructures and mechanical properties of the extruded Mg−11Gd−1Zn alloy [J]. Journal of Alloys and Compounds, 2013, 550: 273−278.
[15] ZENG X Q, WU Y J, PENG L M, LIN D L, DING W J, PENG Y H. LPSO structure and aging phases in Mg−Gd−Zn−Zr alloy [J]. Acta Metallurgica Sinica, 2010, 46(9): 1041−1046.
[16] HOMMA T, KUNITO N, KAMADO S. Fabrication of extraordinary high-strength magnesium alloy by hot extrusion [J]. Scripta Materialia, 2009, 61(6): 644−647.
[17] KAWAMURA Y, YAMASAKI M. Formation and mechanical properties of $Mg_{97}Zn_1RE_2$ alloys with long-period stacking ordered structure [J]. Materials Transactions, 2007: 48(11): 2986−2992.
[18] YAMASAKI M, SASAKI M, NISHIJIMA M, HIRAGE K, KAWAMURA Y. Formation of 14H long period stacking ordered structure and profuse stacking faults in Mg−Zn−Gd alloys during isothermal aging at high temperature [J]. Acta Materialia, 2007, 55(20): 6798−6805.
[19] SCHAFFER J P. The science and design of engineering materials [M]. Beijing: Machinery Industry Press, 2003: 507.
[20] WANG X M, ZENG X Q, ZHOU Y, WU G S, YAO S S, LAI Y J. Early oxidation behaviors of Mg−Y alloys at high temperatures [J]. Journal of Alloys and Compounds, 2008, 460(1−2): 368−374.
[21] LIU M, SCHMUTZ P, UGGOWITZER P J, SONG G, ATRENS A. The influence of yttrium (Y) on the corrosion of Mg−Y binary alloys [J]. Corrosion Science, 2010, 52(11): 3687−3701.
[22] BIRBILIS N, CAVANAUGH M K, SUDHOLZ A D, ZHU S M, EASTON M A, GIBSON M A. A combined neural network and mechanistic approach for the prediction of corrosion rate and yield strength of magnesium−rare earth alloys [J]. Corrosion Science, 2011, 53(1): 168−176.
[23] SONG Y W, SHAN D Y, CHEN R S, HAN E H. Corrosion characterization of Mg−8Li alloy in NaCl solution [J]. Corrosion Science, 2009, 51(5): 1087−1094.
[24] GUO Xue-feng, YANG Wen-peng. Microstructures of Mg−Zn−Y−Ce alloys [M]. Xuzhou: China University of Mining and Technology Press, 2012: 49−50. (in Chinese)
[25] MAO Wei-min, ZHU Jing-chuan, LI Jian, LONG Yi, FAN Qun-cheng. The structure and properties of metallic materials [M]. Beijing: Tsinghua University Press, 2008: 418−422. (in Chinese)
[26] ITOI T, INAZAWA T, YAMASAKI M, KAWAMURA Y, HIROHASHI M. Microstructure and mechanical properties of Mg−Zn−Y alloy sheet prepared by hot-rolling [J]. Materials Science and Engineering A, 2013, 560: 216−223.
[27] TONG L B, LI X H, ZHANG H J. Effect of long period stacking ordered phase on the microstructure, texture and mechanical properties of extruded Mg−Y−Zn alloy [J]. Materials Science and Engineering A, 2013, 563: 177−183.

铸态 Mg−Zn−Y−(Gd)合金凝固组织、腐蚀性能和力学性能

史 菲[1]，王春青[1,2]，张忠明[3]

1. 哈尔滨工业大学(威海) 材料科学与工程学院，威海 264209；
2. 哈尔滨工业大学 先进焊接与连接国家重点实验室，哈尔滨 150001；
3. 西安理工大学 材料科学与工程学院，西安 710048

摘 要：采用常规凝固技术在 $Mg_{94}Zn_3Y_xGd_{3-x}$(x=3，2，1.5，1，摩尔分数)镁合金中获得具有长周期堆垛有序(LPSO)结构相，并对合金凝固组织、耐腐蚀性能和压缩力学性能进行系统研究。结果表明：n(Zn)/n(Y+Gd)=1:1 的 $Mg_{94}Zn_3Y_xGd_{3-x}$ 合金凝固组织含有 α(Mg)相、$Mg_3Zn_3RE_2$(W)相、14H-LPSO 相和少量颗粒状面心立方结构的 Mg−Y−Gd 相。Gd 含量显著影响合金中 LPSO 相的形成和分布。随着 Gd 含量增加，合金中 14H-LPSO 相体积分数先增加后减少。结合电化学阻抗谱分析，LPSO 增强 Mg−Zn−Y−(Gd)镁合金在 3.5% NaCl 溶液中的电化学腐蚀等效电路为 R(Q(R(QR)))。4 种合金的腐蚀电流密度在 10^{-5}A/cm^2 数量级。当 x(Gd)≤1%时，Mg−Zn−Y−(Gd)合金表现出良好的耐蚀性，并优于工业用 AZ91D 镁合金。而当 x(Gd)≥1.5%时，合金的耐腐蚀能力下降。在室温条件下，随着 14H-LPSO 相体积分数增加，Mg−Zn−Y−(Gd)合金的压缩力学性能显著提高。此外，适量 W 相和弥散分布块状 Mg−Y−Gd 相的钉扎作用有利于提高合金的力学性能。

关键词：铸造镁合金；Mg−Zn−Y−(Gd)合金；14H-LPSO 相；腐蚀性能；压缩性能

(Edited by Yun-bin HE)